CHINESE OPTICS LETTERS

Vol. 19, No. 4 | April 2021

Simultaneous measurement of strain and temperature using Fabry–Pérot interferometry and antiresonant mechanism in a hollow-core fiber

Chong He (何 冲)†, Cheng Zhou (周 程)†, Qian Zhou (周 倩)†, Shiyi Xie (谢诗逸), Mengzhe Xiao (肖梦哲), Jiajun Tian (田佳峻)*, and Yong Yao (姚 勇)

School of Electronics and Information Engineering, Harbin Institute of Technology, Shenzhen 518055, China

*Corresponding author: tianjiajun@hit.edu.cn

Received June 20, 2020 | Accepted October 9, 2020 | Posted Online January 4, 2021

A fiber-optic sensor for the simultaneous measurement of strain and temperature is proposed and experimentally demonstrated based on Fabry–Pérot (FP) interference and the antiresonance (AR) mechanism. The sensor was implemented using a single-mode fiber (SMF)–hollow-core fiber–SMF structure. A temperature sensitivity of 21.11 pm/°C was achieved by tracing the troughs of the envelope caused by the AR mechanism, and a strain sensitivity of 2 pm/με was achieved by detecting the fine fringes caused by the FP cavity. The results indicate that the dual-parameter sensor is stable and reliable.

Keywords: fiber-optic sensor; Fabry–Pérot interference; antiresonance.

DOI: 10.3788/COL202119.041201

1. Introduction

Fiber-optic strain sensors have demonstrated their potentials in structural health monitoring[1–3] because they are small in size, corrosion-resistant, immune to electromagnetic interference, and highly sensitive compared with the traditional ones based on mechanical and electronic technologies[4–8]. However, strain measurements are prone to being affected by changes in the ambient environment such as temperature fluctuations. Many methods have been proposed for avoiding temperature crosstalk[9–11], and, in practical applications, these often involve the simultaneous measurement of temperature and strain. One of the most common techniques for simultaneous measurement of strain and temperature involves cascaded structures such as inline interference structures cascaded with polarization-maintaining fibers and multimode fibers[12], cascaded gratings[13–15], cascaded Fabry–Pérot (FP) interferometers (FPIs)[16–18], and in-line modal interferometers[19–21]. These sensors perform simultaneous measurement using a crossing-matrix method and phase demodulation based on path-matching interferometers. Nevertheless, such structures are large, complex, difficult to fabricate, and fragile. Therefore, a structure or mechanism is needed to overcome these shortcomings.

Antiresonance (AR) is generated through an AR reflecting fiber—a photonic bandgap waveguide with a core of low refractive index[22], the thickness of the layer with high refractive index, and the refractive index itself, which dominate the corresponding spectral characteristics [23]. With the introduction of the AR reflecting optical waveguide (ARROW) model[22], the AR reflecting fiber has been gradually applied in the field of optical fiber sensing. Various structures of AR reflecting fibers have been reported, such as photonic crystal fibers[24–26], Kagome fibers[27,28], hollow-core fibers (HCFs) with two eccentric cores[29,30] for temperature[29,31], pressure[32], and curvature[30] sensing, and simple HCFs[23,31,32]. However, most of these approaches can only achieve the measurement of a single parameter by directly tracing the shift of the transmission spectrum based on the AR mechanism. Therefore, temperature crosstalk in complex environments cannot be avoided. In fact, FP interference along the axial direction is ignored by these approaches, because it is too weak in forward transmission as a result of the large amplitude difference between the two forward beams on the two reflecting surfaces in the FP interference. However, it could potentially be used for double-parameter sensing. In the process of reflection, FP interference is dominant in a relatively short HCF, and AR is only generated when the length of the HCF is greater than a critical length. As a result, the reflection spectrum is comprised of spectral components caused by FP interference and AR if an HCF is long enough, and this can be utilized for double-parameter sensing.

In this Letter, a dual-parameter fiber-optic sensor simultaneously measuring strain and temperature is proposed. The sensor works properly with the help of FP interference and AR mechanisms within the AR reflecting fiber constructed from single-mode fiber (SMF)–HCF–SMF. The specific structure comprises an axial FP cavity formed by the hollow core and a radial FP

cavity by the cladding of an HCF, in which the FP interference and AR are generated. It is observed that the reflection spectra are composed of an FP-modulated AR envelope. Since the FP and AR mechanisms within the HCF are solely sensitive to strain and temperature, respectively, this configuration allows the proposed sensor to perform simultaneous measurement. To the best of our knowledge, this is the first time that a combination of FP interference and AR mechanism in an AR reflecting fiber has been applied to the simultaneous measurement of strain and temperature.

2. Sensor Structure and Working Principle

The proposed sensor was composed of an HCF, the cladding thickness and outer diameter of which were 25 μm and 125 μm, respectively. The HCF was sandwiched between two SMFs to form an AR reflecting fiber, as shown in Fig. 1(a). Several steps including fiber cleaving and splicing were required to prepare the proposed sensor. First, two SMFs were spliced onto each end of an HCF (TSP050150, Polymicro Technologies, USA), respectively, with a fiber splicer (FSM-80S, Fujikura, Japan). Second, the fabricated fiber segment was placed under a microscope, and an HCF of the desired length to form the cavity was cleaved. Finally, another SMF was spliced onto the HCF obtained from the second step. The fabricated sensor is exhibited in Fig. 1(b), together with the end face of the HCF used in the experiment.

Regarding the HCF part illustrated in Fig. 1(a), it has a length of L and consists of an air core with a refractive index of n_0 and a cladding of n_2. $2r$ is the inner diameter, and d is the cladding thickness. Likewise, n_1 denotes the refractive index of the core and n_2 the cladding for the SMF. The air cavity between the interface of SMF1 and HCF (M1) and the interface of HCF and SMF2 (M2) forms an axial FPI. In the case of an FPI that

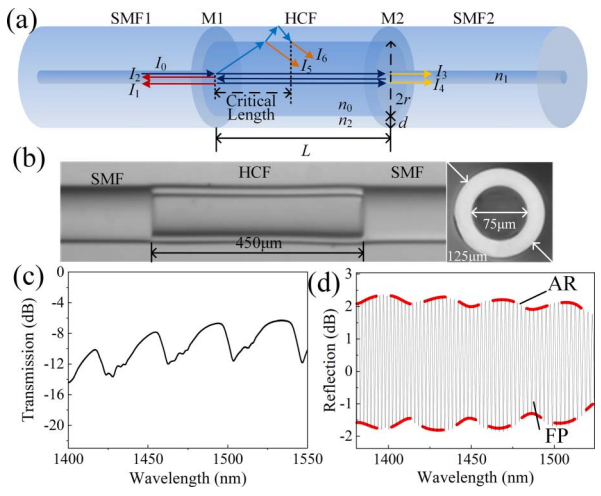

Fig. 1. (a) Schematic of the proposed sensor; (b) typical microscopic image of the fabricated sensor and the HCF cross section; (c) transmission spectrum of a sensor with an HCF of 2050 μm in length; (d) reflection spectrum of a sensor with an HCF of 450 μm in length.

is made of optical fibers, its reflection spectrum is simplified to superposition of I_1 reflected back from M1, and I_2 reflected back from M2 as a result of low reflectivity at each interface. Similarly, its transmission spectrum can also be assumed to be the interference between first transmitted light I_3 and second transmitted light I_4. However, after being reflected twice by M1 and M2, the intensity of I_4 is too weak to form interference with I_3. Therefore, the FP interference is quite weak in transmission, and FP interference was not observed in the structure.

The AR mechanism in the SMF–HCF–SMF structure can be interpreted by the ARROW model[22]. According to this model, the capillary can be considered an FPI along the radial direction, in which the inner wall and outer wall of cladding make up the silica FPI generating AR. The typical resonant wavelengths λ_m can be given as[22]

$$\lambda_m(\mathrm{AR}) = \frac{2d}{m}\sqrt{n_2^2 - n_0^2}, \tag{1}$$

where m denotes the resonant order. The wavelengths of peak intensity for the axial FPI are known as[23]

$$\lambda_m(\mathrm{FP}) = \frac{2L}{m} n_0. \tag{2}$$

A transmission spectrum of the proposed sensor with an HCF of 2050 μm in length is shown in Fig. 1(c). This shows that sharp dips occur at the resonant wavelengths of AR and indicates that FP interference is weak enough to be ignored in the forward propagation. The transmission energy of the AR mechanism will also be reflected by M2. However, AR mechanisms take effect and contribute to the reflection spectrum only if the HCF is longer than a certain length because AR is the result of the interference of two beams—the first reflected light at the air–silica interface, I_5, and the light reflected back from the silica–air interface, I_6 [see Fig. 1(a)]. The periodic dips in the AR spectrum can be interpreted as constructive interference formed in the HCF cladding. The critical length for AR generation is written as[23]

$$L_c = \sqrt{n_0^2 + n_2^2 - n_1^2}\left(\frac{r}{\sqrt{n_1^2 - n_2^2}} + \frac{2d}{\sqrt{n_1^2 - n_0^2}}\right). \tag{3}$$

Therefore, AR and FP interference both contribute to the reflection spectrum if the critical condition, $L \geq L_c$, is satisfied, resulting in a superposed reflection spectrum by axial FP and AR. The superposition is expected to achieve the fine fringes modulated by a broad envelope. The corresponding reflection spectrum is shown in Fig. 1(d), where the HCF was 450 μm in length, and the red dotted lines show the extracted envelope caused by AR, between which the high-frequency fine fringes caused by FP interference are.

In this sensor, these two mechanisms, axial FP interferometry and the AR mechanism, are used to measure strain and temperature. For an FPI sensor, the sensitivity for a physical quantity X is given by

$$\frac{\Delta\lambda}{\Delta X}=\lambda\left(\frac{1}{n}\frac{\Delta n}{\Delta X}+\frac{1}{L}\frac{\Delta L}{\Delta X}\right). \tag{4}$$

Since the refractive index variation of air is negligible when the temperature changes compared to that of silica[33], it is convenient to obtain the temperature dependence of the sensor by leaving out the air index variation, which can be derived from Eq. (1), expressed as

$$\frac{\partial\lambda_m(\mathrm{AR})}{\partial T}=\frac{2dn_2}{m\sqrt{n_2^2-n_0^2}}\frac{\partial n_2}{\partial T}, \tag{5}$$

where $\partial n_2/\partial T$ is the thermo-optic coefficient of cladding material of HCF.

The cavity length of an FPI varies with the axial strain applied to it. However, L has no effect on $\lambda_m(\mathrm{AR})$ according to Eq. (1). Therefore, only the fine fringes of the reflection spectra in FP interference will shift when the strain changes. The strain sensitivity S of an FP cavity can be expressed as[9]

$$S=k_\varepsilon\frac{L_{\mathrm{FP}}+L_{\mathrm{SMF}}}{L_{\mathrm{SMF}}\frac{A_{\mathrm{FP}}}{A_{\mathrm{SMF}}}+L_{\mathrm{FP}}}, \tag{6}$$

where k_ε is the strain coefficient, L_{FP} and L_{SMF} are the lengths of the HCF and SMF, respectively, and A_{FP} and A_{SMF} are the cross-sectional areas of the HCF and SMF, respectively. From this equation, if A_{FP} is smaller than A_{SMF}, then the strain sensitivity will increase with decreasing L_{FP}. It should be noted that a longer air-cavity FPI reduces the visibility of the interference fringes because of greater losses, whereas AR is generated only if the length of HCF is greater than the critical length. Furthermore, the critical length and the strain sensitivity both increase as the thickness of the HCF decreases. Therefore, there is a tradeoff between the fringe visibility and the strain sensitivity of the sensor.

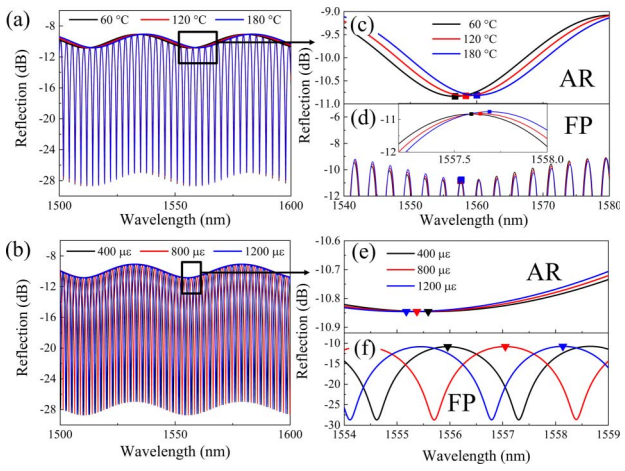

Fig. 2. Calculated spectra of the proposed sensor with different temperature and strain. (a), (b) Reflection spectra with increasing temperature and strain, respectively; (c)–(f) AR envelopes and FP fringes under different temperature and strain.

To study the effect of temperature and strain acting on the sensor, theoretical calculations were conducted[16,23]. Figures 2(a) and 2(b) show the calculated reflection spectra of the proposed sensor under different temperature and strain, respectively. Specifically, Figs. 2(c) and 2(d) show the spectra with the increased temperature, where the AR envelope has a red shift of 25 pm/°C, while the FP fringe response for temperature is only 0.7 pm/°C. Using the same analysis for strain tests, FP fringes evidently shift toward longer wavelengths with a strain response of 2.7 pm/με, while a response −0.52 pm/με is obtained from the AR envelope, as shown in Figs. 2(c) and 2(d). Consequently, it is acceptable to assume, in principle, that the AR envelope is solely sensitive to temperature, and the FP fringe is solely sensitive to strain.

3. Experiments and Results

3.1 Temperature measurement

Figure 3 exhibits an experimental setup for the purpose of testing the temperature responses, where a broadband light source (BBS, ASE, FiberLake, China) was connected to Port 1 of the optical circulator (OC), the fabricated sensor to Port 2, and the optical spectral analyzer (OSA, AQ6370C, Yokogawa, Japan) to Port 3. The light over a wavelength range 1250–1650 nm from the BBS was launched in the sensor and finally reflected back into the OSA and recorded. The sensor was placed in an oven (SG XL 1200, SIOM, China) that increased the temperature from 40°C to 190°C at intervals of 20°C. The sensor was not subject to external forces during the temperature test.

The AR envelope was extracted by linking the highest or lowest points of each peak or valley in the reflection spectrum of the sensor. Figure 4(a) shows the evolution of one dip of the extracted envelope with increasing temperature, where the spectrum shifts towards longer wavelengths. Figure 4(b) shows the evolution of the FPI fine fringes with respect to temperature. It indicates that the temperature does not influence the FP fringes of the sensor. The results are consistent with the calculations. By tracing the dips of the envelope in Fig. 4(a), the temperature-induced wavelength shift was obtained and is plotted in Fig. 4(c), where a linear relationship is demonstrated. The temperature sensitivity of the AR mechanism was 21.11 pm/°C, and the temperature response of the FP fringe was estimated to be 0.35 pm/°C.

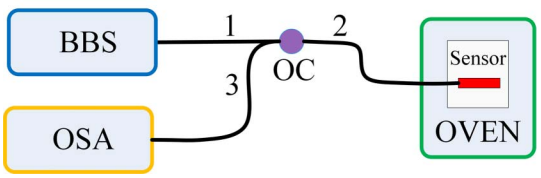

Fig. 3. Experimental setup for temperature measurement.

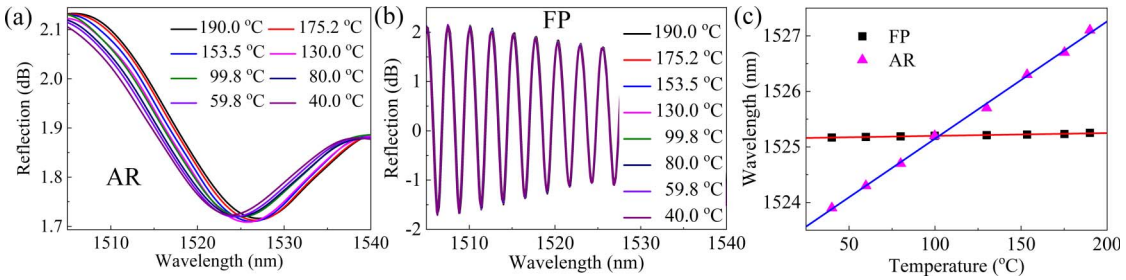

Fig. 4. (a) Dip of AR envelope with increasing temperature; (b) FP fringes with increasing temperature; (c) wavelength shift of AR envelope and FP fringe versus temperature.

3.2 Strain measurement

The strain responses were also investigated with the experimental setup described in Fig. 5. Two ends of fibers that connect the sensor were fixed on a fiber-optic platform and a translation stage with glue, respectively, and the distance between two fixed points was set to 25 cm. The length of the fiber between the two glued points was gradually increased by changing the axial position of the translation stage. The extended length was increased from 5 μm to 300 μm with steps of 50 μm, and the reflection spectrum was recorded immediately in each step. The longitudinal strain ε was calculated using

$$\varepsilon = \frac{\Delta L}{L'}, \tag{7}$$

where L' is the original length between two fixed points, and ΔL is the extended length in the axial direction. From Eq. (7), the longitudinal strain ε that was applied to the sensor was increased from 0 to 1200 με with steps of 200 με. During the strain test, the temperature was maintained at 25°C.

Figure 6(a) shows a single valley of the AR envelopes under different strains, from which a clear red shift in the FPI fine fringes occurs as the strain is increased. This is because when the axial strain is applied to the sensor, the cavity length of the axial FPI increases. According to Eq. (2), the reflection spectrum should shift toward longer wavelengths with the increasing FP cavity length L. A linear relationship between the strain and the wavelength shift was found, as shown in Fig. 6(c), and the sensitivity of the FPI was 2 pm/με. Additionally, the strain response of the AR envelope was calculated to be −0.55 pm/με. Therefore, compared to the temperature responses, the AR envelope experienced a little movement with changes in strain, and only the amplitude changed as a result of the drift in the FPI spectrum, as shown in Fig. 6(b), which coincides with the calculations.

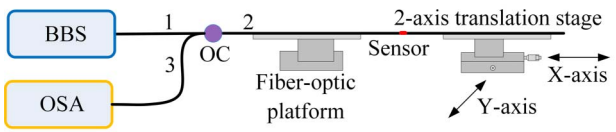

Fig. 5. Experimental setup for strain measurement.

3.3 Validity analysis

The temperature and strain responses of the sensor envelope will not be affected because the measurement mechanisms of the two

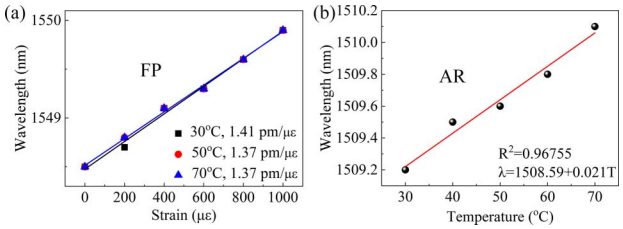

Fig. 7. (a) Strain response of the proposed sensor at 30°C, 50°C, and 70°C by tracing FP fringe wavelength shift; (b) temperature response of the proposed sensor at specific strain by tracing AR envelope wavelength shift.

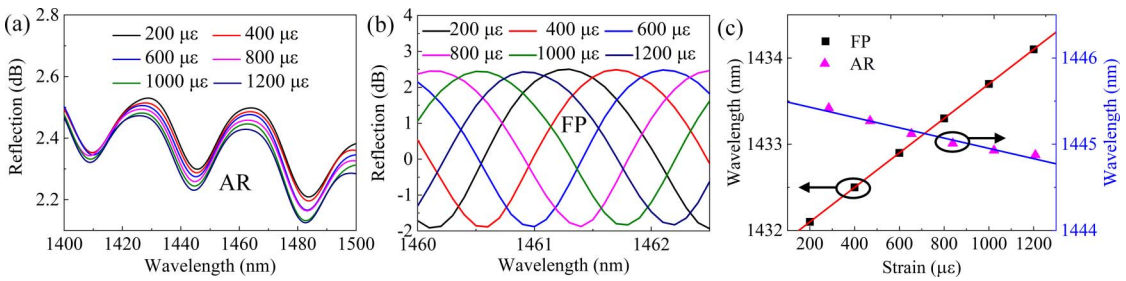

Fig. 6. (a) Typical AR envelope of the sensor under different strains; (b) FP fringe under different strains; (c) FP fringe and AR envelope wavelength shift at different strains.

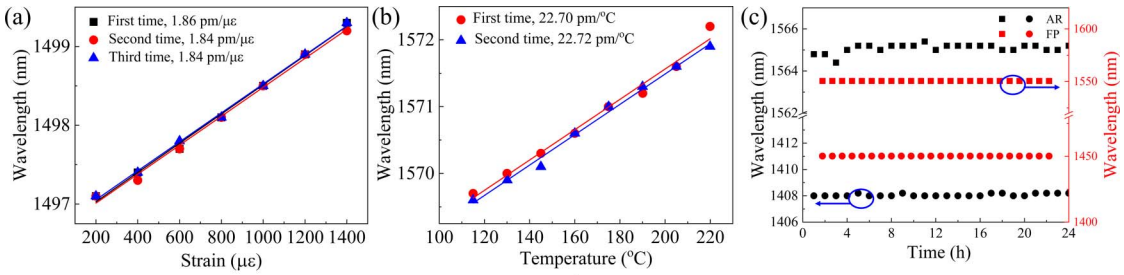

Fig. 8. (a) Strain repeatability of the experimental result from the proposed sensor by tracing FP fringe wavelength shift; (b) temperature repeatability of the experimental result from the proposed sensor by tracing the AR envelope wavelength shift; (c) long-time stability of the AR mechanism and the FP interference.

parameters are independent. To experimentally demonstrate this, another sensor was fabricated from an HCF with a length of 600 μm and the inner and outer diameters of 75 and 125 μm, respectively. Two ends of the sensor were fixed to the translation stages, and a heating platform was placed below it so the ambient temperature of the sensor could be changed. When the temperature reached 30°C, 50°C, and 70°C, the position of the translation stage was changed to apply strain to the sensor, and the applied strain range was 0–1000 με. The spectra were recorded with a step of 200 με. The strain response curves at three different temperatures are shown in Fig. 7(a), and the sensitivities of the sensor at these different temperatures were 1.41, 1.37, and 1.37 pm/με, respectively, which indicates that the measurement of strain is independent of temperature. Figure 7(b) shows temperature responses of the AR envelope during the strain test when the applied strain was 200 με, the result of which was estimated to be 21 pm/°C.

A simultaneous measurement of strain and temperature is allowed by comparing the reflection spectra detected in changing environmental conditions to the original calibration one. This scheme works because the FP- and AR-based spectra are almost solely sensitive to their specific measurements, the corresponding crosstalk of which was estimated to be 0.026°C/με for the AR envelope and 0.175 με/°C for the FP fringe.

3.4 Repeatability and stability

To investigate the repeatability of the proposed sensor, we conducted three temperature and strain experiments, each separated by 3 h, using a sensor with an HCF 445 μm in length. Strain measurement was found to be repeatable, as shown in Fig. 8(a), and the repeatability error was estimated to be 0.54%. The strain sensitivities from the three separate tests were 1.86, 1.84, and 1.84 pm/με. The temperature sensitivities, calculated for two tests, were 22.70 and 22.72 pm/°C, indicating good repeatability, as illustrated in Fig. 8(b).

The temporal stability of the proposed sensor was also investigated. Measurements were taken continuously for 24 h under the same temperature and strain conditions. The spectral changes in the AR envelope of the sensor's reflectance spectrum around 1408 and 1565 nm and the spectral fringe changes in the FPI spectrum around 1450 and 1550 nm are shown in Fig. 8(c). The positions of the two troughs in the AR envelope varied by 0.2 and 0.4 nm, respectively, whereas the positions of the two troughs in the FP spectrum were almost constant, demonstrating that the strain measurement obtained from FP interference is extremely stable.

4. Conclusion

In summary, we have proposed and demonstrated an FP- and AR-based dual-parameter sensor with an SMF–HCF–SMF configuration. This system can simultaneously measure strain and temperature due to different spectral sensitivities of FP interference and AR mechanism, which occurr in the air core and cladding, respectively, to strain and temperature. The experimental results show that the temperature sensitivity of our system was 21.11 pm/°C, and the strain sensitivity was 2 pm/με. The corresponding crosstalk was 0.026°C/με and 0.175 με/°C. Moreover, the proposed sensor is small, simple, robust, and reliable, making it a good candidate for structural health monitoring of buildings, tunnels, and many other structures.

Acknowledgement

This work was financially supported in part by the National Natural Science Foundation of China (No. 61675055) and the Shenzhen Municipal Science and Technology Plan Project (Nos. JCYJ20170815140136635 and JCYJ20190806143818818).

†These authors contributed equally to this work.

References

1. H. Guo, G. Xiao, N. Mrad, and J. Yao, "Fiber optic sensors for structural health monitoring of air platforms," Sensors **11**, 3687 (2011).
2. H. Murayam, D. Wada, and H. Igawa, "Structural health monitoring by using fiber-optic distributed strain sensors with high spatial resolution," Photon. Sens. **3**, 355 (2013).
3. H. Pei, J. Teng, J. Yin, and R. Chen, "A review of previous studies on the applications of optical fiber sensors in geotechnical health monitoring," Measurement **58**, 207 (2014).
4. S. Liehr, P. Lenke, M. Wendt, K. Krebber, M. Seeger, E. Thiele, H. Metschies, B. Gebreselassie, and J. C. Münich, "Polymer optical fiber sensors for distributed strain measurement and application in structural health monitoring," IEEE Sens. J. **9**, 1330 (2009).

5. X. Liang, T. Ning, J. Li, Y. Li, and Z. Liu, "Axial micro-strain sensor based on resonance demodulation technology via dual-mode CMECF," Photon. Sens. **9**, 78 (2019).
6. C. Lu, J. Su, X. Dong, T. Sun, and K. T. V. Grattan, "Simultaneous measurement of strain and temperature with a few-mode fiber-based sensor," J. Lightwave Technol. **36**, 2796 (2018).
7. C. Lang, Y. Liu, K. Cao, and S. Qu, "Temperature-insensitive optical fiber strain sensor with ultra-low detection limit based on capillary-taper temperature compensation structure," Opt. Express **26**, 477 (2018).
8. J. Tian, Y. Jiao, Q. Fu, S. Ji, Z. Li, M. Quan, and Y. Yao, "A Fabry–Perot interferometer strain sensor based on concave-core photonic crystal fiber," J. Lightwave Technol. **36**, 1952 (2018).
9. M. R. Mokhtar, K. Owens, J. Kwasny, S. E. Taylor, P. A. M. Basheer, D. Cleland, Y. Bai, M. Sonebi, G. Davis, A. Gupta, I. Hogg, B. Bell, W. Doherty, S. McKeague, D. Moore, K. Greeves, T. Sun, and K. T. V. Grattan, "Fiber-optic strain sensor system with temperature compensation for arch bridge condition monitoring," IEEE Sens. J. **12**, 5 (2012).
10. H. Li, Q. Zhao, S. Jiang, J. Ni, and C. Wang, "FP cavity and FBG cascaded optical fiber temperature and pressure sensor," Chin. Opt. Lett. **17**, 040603 (2019).
11. T. Yang, Z. Ran, X. He, Z. Li, Z. Xie, and Y. Wang, "Temperature-compensated multifunctional all-fiber sensors for precise strain/high-pressure measurement," J. Lightwave Technol. **37**, 4634 (2019).
12. R. Xing, C. Dong, Z. Wang, Y. Wu, Y. Yang, and S. Jian, "Simultaneous strain and temperature sensor based on polarization maintaining fiber and multimode fiber," Opt. Laser Technol. **102**, 17 (2018).
13. R. Subramanian, C. Zhu, H. Zhao, and H. Li, "Torsion, strain, and temperature sensor based on helical long-period fiber gratings," IEEE Photonics Technol. Lett. **30**, 327 (2018).
14. X. Jin, C. Sun, S. Duan, W. Liu, G. Li, S. Zhang, X. Chen, L. Zhao, C. Lu, X. Yang, T. Geng, W. Sun, and L. Yuan, "High strain sensitivity temperature sensor based on a secondary modulated tapered long period fiber grating," IEEE Photon. J. **11**, 7100908 (2019).
15. C. Sun, R. Wang, X. Jin, Z. Wang, W. Liu, S. Zhang, Y. Ma, J. Lin, Y. Li, T. Geng, W. Sun, Z. Qu, and L. Yuan, "A new phase-shifted long-period fiber grating for simultaneous measurement of torsion and temperature," Chin. Opt. Lett. **18**, 021203 (2020).
16. J. Tian, Y. Jiao, S. Ji, X. Dong, and Y. Yao, "Cascaded-cavity Fabry–Perot interferometer for simultaneous measurement of temperature and strain with cross-sensitivity compensation," Opt. Commun. **412**, 121 (2018).
17. Z. Ran, C. Li, H. Zuo, and Y. Chen, "Laser-machined cascaded micro cavities for simultaneous measurement of dual parameters under high temperature," IEEE Sens. J. **13**, 1988 (2013).
18. H. Singh and J. S. Sirkis, "Simultaneously measuring temperature and strain using optical fiber microcavities," J. Lightwave Technol. **15**, 647 (1997).
19. Y. Zhao, L. Cai, and X. G. Li, "In-fiber modal interferometer for simultaneous measurement of curvature and temperature based on hollow core fiber," Opt. Laser Technol. **92**, 138 (2017).
20. X. Zhang, C. Liu, J. Liu, and J. Yang, "Single modal interference-based fiber-optic sensor for simultaneous measurement of curvature and strain with dual-differential temperature compensation," IEEE Sens. J. **18**, 8375 (2018).
21. Z. Wu, B. Liu, J. Zhu, J. Liu, S. Wan, T. Wu, and J. Sun, "Asymmetrical tapered SMS fiber coupler for simultaneous measurement of temperature and refractive index and its application for biosensing," Chin. Opt. Lett. **18**, 061201 (2020).
22. N. M. Litchinitser, A. K. Abeeluck, C. Headley, and B. J. Eggleton, "Antiresonant reflecting photonic crystal optical waveguides," Opt. Lett. **27**, 1592 (2002).
23. X. Zhang, H. Pan, H. Bai, M. Yan, J. Wang, C. Deng, and T. Wang, "Transition of Fabry–Perot and antiresonant mechanisms via a SMF-capillary-SMF structure," Opt. Lett. **43**, 2268 (2018).
24. R. Gao, D. Lu, J. Cheng, Y. Jiang, and Z. Qi, "Temperature-compensated fibre optic magnetic field sensor based on a self-referenced anti-resonant reflecting optical waveguide," Appl. Phys. Lett. **110**, 131903 (2017).
25. S. Liu, Y. Wang, M. Hou, J. Guo, Z. Li, and P. Lu, "Anti-resonant reflecting guidance in alcohol-filled hollow core photonic crystal fiber for sensing applications," Opt. Express **21**, 31690 (2013).
26. N. M. Litchinitser, S. C. Dunn, B. Usner, B. J. Eggleton, T. P. White, R. C. McPhedran, and C. M. de Sterke, "Resonances in microstructured optical waveguides," Opt. Express **11**, 1243 (2003).
27. G. J. Pearce, G. S. Wiederhecker, C. G. Poulton, S. Burger, and P. St. J. Russell, "Models for guidance in kagome-structured hollow-core photonic crystal fibres," Opt. Express **15**, 12680 (2007).
28. S. Liu, N. Liu, M. Hou, J. Guo, Z. Li, and P. Lu, "Direction-independent fiber inclinometer based on simplified hollow core photonic crystal fiber," Opt. Lett. **38**, 4 (2013).
29. W. Ni, P. Lu, X. Fu, H. Sun, P. P. Shum, H. Liao, X. Jiang, D. Liu, C. Yang, J. Zhang, and Z. Lian, "Simultaneous implementation of enhanced resolution and large dynamic range for fiber temperature sensing based on different optical transmission mechanisms," Opt. Express **26**, 18341 (2018).
30. W. Ni, P. Lu, J. Zhang, C. Yang, X. Fu, Y. Sun, H. Liao, and D. Liu, "Single hole twin eccentric core fiber sensor based on anti-resonant effect combined with inline Mach–Zehnder interferometer," Opt. Express **25**, 12372 (2017).
31. D. Liu, Q. Wu, C. Mei, J. Yuan, X. Xin, A. K. Mallik, F. Wei, W. Han, R. Kumar, C. Yu, S. Wan, X. He, B. Liu, G. Peng, Y. Semenova, and G. Farrell, "Hollow core fiber based interferometer for high-temperature (1000°C) measurement," J. Lightwave Technol. **36**, 1583 (2018).
32. M. Hou, F. Zhu, Y. Wang, Y. Wang, C. Liao, S. Liu, and P. Lu, "Antiresonant reflecting guidance mechanism in hollow-core fiber for gas pressure sensing," Opt. Express **24**, 27890 (2016).
33. A. Michie, J. Canning, K. Lyytikäinen, M. Aslund, and J. Digweed, "Temperature independent highly birefringent photonic crystal fibre," Opt. Express **12**, 5160 (2004).